Investigation of the effect of the shape of grains on flows inside hoppers

by

Seyyed Hossein Motavali Largichi
B.Sc., I.A.U., 2012

A Report Submitted in Partial Fulfillment
of the Requirements for the Degree of

MASTER OF ENGINEERING

in the Department of Mechanical Engineering

Supervisory Committee

Investigation of the effect of the shape of grains on flows inside hoppers
by

Seyyed Hossein Motavali Largichi
BSc, I.A.U., 2012

Supervisory Committee

Dr. Ben Nadler, (Department of Mechanical Engineering)
Supervisor

Dr. Peter Oshkai, (Department of Mechanical Engineering)
Departmental Member

Abstract

Non-spherical granular flow is strongly affected by the shape of grains. In this project, a numerical analysis is performed for two non-spherical grains such as rice and lentil by applying a kinematic continuum model as the governing equation in rectangular hoppers with two different opening sizes. The kinematic continuum model is based on the velocity field and shape of grains, where the velocity field is provided by experiment and the shape of the grains is characterized by two geometrical dimensions. Results include the orientation field of grains compared to experimental measurements to investigate the performance of the model. It was observed that the orientation of grains is horizontal at the highest layer of the hopper and it changes to vertical as the grains flow closer to the opening. It was observed that the grains were less aligned in the center in comparison to the grains near the walls. Moreover, the grains orient with the streamline, as they flow down. This orientation with the streamline happens at farther upstream for the smaller opening in comparison to the larger opening. However, rice was orienting with the streamline at farther upstream in comparison to lentils in the smaller opening. This can be rooted in having a more ellipsoidal shape for rice compared to lentils. Furthermore, two parameters in the model which are a function of the shape of grains are determined to have a better agreement in terms of the orientation field of grains compared to the experimental measurements.

Supervisory Committee

Dr. Ben Nadler, (Department of Mechanical Engineering)

Supervisor

Dr. Peter Oshkai, (Department of Mechanical Engineering)

Departmental Member

Table of Contents

Supervisory Committee ii
Abstract iii
Table of Contents iv
List of Tables v
List of Figures vi
List of Nomenclatures vii
Acknowledgments ix
Dedication x
Chapter 1 : Introduction 1
Chapter 2 : Computational Analysis 5
2-1 Mathematical Model 5
2-2 Discretization 10
2-3 Numerical Results 14
2-3-1 Initial Condition 14
2-3-2 Visualization of Orientation Distribution of Grains 15
2-3-3 Analyzed Domain 16
2-3-4 Rice 16
2-3-5 Lentil 19
Chapter 3 : Model and Experimental Comparison 22
3-1 Rice Orientation Distribution Comparison 24
3-2 Lentil Orientation Distribution Comparison 27
3-3 Principal Average Orientational Angle Comparison 30
Chapter 4 : Determination of The Model Parameters 33
Chapter 5 : Conclusions 39
Bibliography 40
Appendix 42

List of Tables

Table 1 : Properties of grains used in the experimental setup 9
Table 2 : Comparison between the experimental and model orientation field of grains .. 22
Table 3 : Determination of model parameters for rice and lentil in the hopper with 10 mm or 15 mm openings..... 34

List of Figures

Figure 1 : Visualization of the orientation distribution..... 15
Figure 2 : Orientation field of rice in hopper flow (opening 10 mm)..... 17
Figure 3 : Orientation field of rice in hopper flow (opening 15 mm)..... 18
Figure 4 : Orientation field of lentil in hopper flow (opening 10 mm)..... 20
Figure 5 : Orientation field of lentil in hopper flow (opening 15 mm)..... 21
Figure 6 : Model and experimental comparison of the orientation field for rice (opening 10 mm).. 25
Figure 7 : Model and experimental comparison of the orientation field for rice (opening 15 mm).. 26
Figure 8 : Model and experimental comparison of the orientation field for lentil (opening 10 mm).. 28
Figure 9 : Model and experimental comparison of the orientation field for lentil (opening 15 mm).. 29
Figure 10 : Model and experimental comparison of the average principal orientational angle per height of the hopper for rice.. 31
Figure 11 : Model and experimental comparison of the average principal orientational angle per height of the hopper for lentil..... 32
Figure 12 : Model and experimental comparison of the orientation field for rice with the optimized model parameters (opening 10 mm).. 35
Figure 13 : Model and experimental comparison of the orientation field for rice with the optimized model parameters (opening 15 mm).. 36
Figure 14 : Model and experimental comparison of the orientation field for lentil with the optimized model parameters (opening 10 mm).. 37
Figure 15 : Model and experimental comparison of the orientation field for lentil with the optimized model parameters (opening 15 mm).. 38

List of Nomenclatures

$f(\mathbf{k})$	Probability density function
$\mathbf{k}$	The orientation direction vector of a grain
$\dot{\mathbf{k}}$	The material time derivative of $\mathbf{k}$
$\mathbf{A}$	Second order tensorial moment of orientation distribution
$\dot{\mathbf{A}}$	The material time derivative of $\mathbf{A}$
$\mathbf{A}^{exp}$	Experimental measurement of orientational tensor
$\mathbf{A}^{mod}$	Model orientational tensor
$\mathbf{v}$	Velocity field
$\mathbf{L}$	Velocity gradient
$\mathbf{D}$	The rate of deformation
$\mathbf{D}'$	Deviatoric part of the rate of deformation
$\mathbf{W}$	Vorticity
r_g	The shape of grains characteristic
λ, ψ	Model parameters
ζ	Measurement of grains alignment
x-axis	The axis that is along the length of the hopper
y-axis	The axis that is along the height of the hopper
z-axis	The axis that is along the width of the hopper
θ	The orientation angle of the largest eigenvalue's eigenvector
θ_{ave}	The average orientation angle

θ^{exp}	Experimental measurement of orientational angle
θ^{mod}	Model orientational angle
E_{θ}	Orientation angle error
$E_{\mathbf{A}}$	Orientation tensor error
MATLAB	Multi-paradigm numerical computing environment and proprietary programming language developed by MathWorks

Acknowledgments

Foremost, I would like to express my sincere gratitude to my supervisor Dr. Ben Nadler for the continuous support during my studies, for his patience, motivation, enthusiasm, and immense knowledge. His guidance helped me in all the time of this project and report. I could not have imagined having a better supervisor and mentor for my study.

Besides my supervisor, I would like to thank Dr. Peter Oshkai for teaching Computational fluid dynamics and fluid mechanics courses, and encouragement comments in the supervisory committee.

I thank my friend Yaser Mohammadi for simulation discussions.

Last but not least, I would like to thank my parents, my sister, my wife Raheleh Akbari and my uncle Mehdi Motewelli who support me spiritually throughout my life and studies.

Dedication

Dedicated to my parents, sister, wife, and uncle

Chapter 1 : Introduction

Non-spherical granular flows are ubiquitous in industries such as agriculture, food processing, where crops have elongated or flattened shapes, and pharmaceutics with pills and drug capsules. The significance of non-spherical granular flow inside hopper was examined both experimentally and numerically to study various aspects such as the effect of the shape of grains on hopper flow, the modeling of the shape irregularity of grains, and the effect of the shape of grains on jamming probability [1-6].

In [1], a research group at the University of Sydney conducted an experiment to study spherical and non-spherical granular flows inside hoppers in order to measure velocity field, internal size, and orientation of grains by means of dynamic X-ray radiography. The rectangular hopper has the height of 300 mm, width of 150 mm, and length of 130 mm with two different opening sizes. The opening is a rectangle, which has one dimension the same as the width of the hopper and one variable dimension including 10 mm, 12 mm, and 15 mm. In this experiment, glass beads were used as the spherical grains and jasmine rice and red lentils as the non-spherical grains. The properties of grains such as the minor and major axis were measured by micrometer and X-ray density wavelength. It was reported that previous popular techniques for tracking internal deformations in granular materials include X-ray computed tomography (X-ray CT), Positron Emission Particle Tracking (PEPT), Magnetic Resonance Imaging (MRI), Refractive Index-Matched Scanning (RIMS), which have associated disadvantages such as safety, cost, spatial, and temporal resolution. X-ray CT is the most popular technique, which is restricted to discontinuous flows since it needs several consecutive loading steps for proper radiographic scanning around a sample. However, RIMS is a good technique for continuous flows, but it needs the use of an interstitial fluid with a refractive index matched to the investigated grains, which affect the nature of granular flow. Due to these limitations, it was more reasonable to study only part of the velocity field by taking images along free surfaces and then analyzing the images by Particle Image Velocimetry (PIV) and Fourier transformation. In the experiment, the hopper was filled with grains and discharge was initiated by releasing a trapdoor mechanism. After a brief transient period, the material discharges at a constant

rate. Temporal averages of the measured values of the fabric and velocity fields were performed during this phase of constant discharge rate. X-ray radiography was used to image the flow of grains inside the hopper. A Spellman XRV generator was used to emit X-ray radiation at certain maximum energy and intensity for glass beads, rice, and lentils. The radiation passed through granular medium and the transmitted component was recorded on a PaxScan 2520DX detector at 960 × 768 pix resolution and at 30 frames per second. It was observed that both funnel and mass flow regimes depend on the material and opening size, which funneling tending to be stronger for smaller openings and non-spherical grains. The glass beads flow uniformly in a relatively constant manner over time, whereas the flow for the elongated grains exhibits some transient instability. Moreover, the grain size was measured both by micrometer with randomly selecting 20 grains from each type and the experimental technique. The results from both methods showed good agreement. Furthermore, the orientation of grains was measured using X-ray radiography and Fourier transforms, and steel tracer particles. The steel tracer particles have the same size of the grains and they are placed every 2 cm above one another vertically in the center of the hopper. The results for both cases showed that the experiment technique is able to measure the orientation of grains in space and time. It was observed that the average orientation of rice or lentils is horizontal at the highest layer of the hopper, where the grains place horizontally and as rice or lentils flow down, the average orientation of rice or lentils changes to vertical closer to the opening. Moreover, in [2], an experimental consideration was performed on a cylindrical hopper with changeable opening size in the center of the bottom plane. The hopper was filled and tested for various elongated grains such as pegs and flat lentils and closely spherical-shape grains like peas using x-ray tomography to find the effect of the shape of grains on the hopper flow. It was found that the more elongated grains show a preferred orientation with a greater ordering in the flowing zone. The average orientation of grain is almost parallel to the streamline with a certain angle deviation as similar to the simple shear flows. In [3], a numerical analysis was performed on rounded-cap rectangular (RCR) grains, which is characterized by the shape aspect ratio to study the effect of elongated grains on the behavior of sheared granular material. An elongation parameter was defined, which is differed between 0 and 1 as the grains vary from a circle to a thin line, respectively. The RCR grains were simulated by contact dynamic method,

where it was assumed that there are three types of contacts between grains such as cap-to-cap, cap-to-side, and side-to-side. It was found that the increasing mobilization of friction force and associated anisotropy are the key effects of grain elongation. The force and grain's anisotropy lead to the increase of shear strength and the increase of friction force. In [4], the shape irregularity of Toyoura sand was modeled by District Element Method simulations (DEM) and compared with the experimental measurements to assess the accuracy of the modeling. This is performed since grains used in industries have an irregular shape and this affects granular flows. Two types of modeling were conducted to study the accuracy of the number of spherical element used in the modeling of the shape irregularity including modeling with 4 and 10 spherical elements. Various 3-D DEM simulations of simple shear were performed and results were compared with experimental tests on Toyoura sand and the accuracy of the modeling was evaluated. It was found that the accuracy of the modeling is based on the number of elements that are used for modeling, where modeling with 10 spherical elements showed better agreement with the experimental tests.

In [5], an experimental study was conducted on the jamming probability of spherical and non-spherical grains in the cylindrical hopper with a circular opening at the bottom. It was found that there is a critical radius for the opening, which above this radius clogging will not occur. The opening critical radius was measured for spherical grains and found that it is constant for different grain with the same grain's radius. However, if the grains are non-spherical, there is a critical radius for the opening, which is based on the ratio of opening's radius and grain's radius. It was found that grain's material properties such as density and elasticity have no effect on the jamming probability. Whereas, the shape of grains affects the formation of the arch, and then the probability of jamming. Moreover, in [2], It was found that the jamming probability is characterized by the arch, which is formed by the grains to block the discharge and the shape of the arch depends on the grain's shape. In [6], a rotating 2-D hopper that is filled with polished disks and unpolished disks was considered. It was found that there is a relation between jamming probability and opening size that as the ratio of opening's diameter and grain's diameter increases, the jamming probability decreases.

In this report, a numerical analysis using a kinematic continuum model is performed in hoppers with similar properties as [1]. The hoppers are filled with rice and lentils. The model is based on the velocity field and shape of grains, and it is applied only to the center of the hoppers to avoid the stagnation zones. The velocity field and position of grains in the hoppers are given by experiment. The orientation field of grains at the highest layer of the domain is considered to be only in the length and width plane of the hopper as initial conditions for solving the model in the domain. The initial conditions used in the model are similar to the experiment. The results include the orientation angle and orientation field of grains were visualized and compared to the experimental measurements to investigate the performance of the model. Moreover, two model parameters are determined to have a better agreement in terms of the orientation field of grains in the domain compared to the experimental measurements.

Chapter 2 : Computational Analysis

2-1 Mathematical Model

Available mathematical models are specific to spherical grains, where the lack of a mathematical model to predict the behavior of non-spherical grains was observed. The difficulty is that in non-spherical grains, grains arrangement has a considerable effect on mechanical properties. Therefore, a kinematic continuum model, which depends on the velocity field and shape of grain was proposed to predict the orientation and alignment of non-spherical grains. The kinematic continuum model was compared to simple shear District Element Method simulations (DEM) showing good agreement in either steady-state and transient flows.

To represent non-spherical grains, there should be 2-D close surface representations for identifying a shape [7-11]. It is assumed that simple extension through a single parameter of spherical grain results in an ellipsoidal shape. Therefore, any axisymmetric grains can be described by two geometrical dimensions and a unique orientation direction.

The statistical orientation of grains at a given point in space and time can be represented by a probability density function f (**k**), where f (+ **k**) = f (– **k**) ≥ 0 and

$$\oint_{s^2} f(\mathbf{k})\, da = 1 , \tag{2.1}$$

where **k** is the orientation direction vector and s^2 is unit sphere.

The simplest model used a second order orientational tensor is considered for the representation of orientation distribution of grains instead of f (**k**) as

$$\mathbf{A} = \oint_{s^2} f(\mathbf{k})\, \mathbf{k} \otimes \mathbf{k}\, da . \tag{2.2}$$

By taking the transpose of second order orientational tensor in equation (2.2), it will be realized that **A** is symmetric as

$$\mathbf{A}^{T} = (\oint_{s^2} f(\mathbf{k})\, \mathbf{k} \otimes \mathbf{k}\, da)^{T} = \oint_{s^2} f(\mathbf{k})\, \mathbf{k} \otimes \mathbf{k}\, da = \mathbf{A}\,. \tag{2.3}$$

A is a positive semi-definite tensor ($\mathbf{b} \cdot \mathbf{A}\, \mathbf{b}) \geq 0$, where **b** is any non-zero vector. This is outlined as $\mathbf{b} \cdot (\oint_{s^2} f(\mathbf{k})\, \mathbf{k} \otimes \mathbf{k}\, da)\, \mathbf{b}$. Since **b** is not a function of **k**, it is brought into the integral and it is simplified to

$$\oint_{s^2} f(\mathbf{k})\, \mathbf{b} \cdot \mathbf{k} \otimes \mathbf{k} \cdot \mathbf{b}\, da = \oint_{s^2} f(\mathbf{k})\, (\mathbf{k} \cdot \mathbf{b})^2\, da\,, \tag{2.4}$$

where $f(\mathbf{k}) \geq 0$ and $(\mathbf{k} \cdot \mathbf{b})^2 \geq 0$. Therefore, $(\mathbf{b} \cdot \mathbf{A}\, \mathbf{b}) \geq 0$ that shows **A** is a positive semi-definite tensor.

Since **A** is symmetric, the spectral representation of **A** can be expressed as

$$\mathbf{A} = \sum_{i=1}^{3} \lambda_i\, (\mathbf{e}_i \otimes \mathbf{e}_i)\,, \tag{2.5}$$

where λ_i are eigenvalues and $0 \leq \lambda_i \leq 1$ and $\mathbf{e}_i$ are the associated eigenvectors.

A measurement of grains alignment (ζ) was proposed as

$$\zeta = \sqrt{\frac{1}{2}\,((\lambda_1 - \lambda_2)^2 + (\lambda_2 - \lambda_3)^2 + (\lambda_3 - \lambda_1)^2)}\,, \tag{2.6}$$

where $0 \leq \zeta \leq 1$. In the limit cases, $\zeta = 0$ if and only if the orientation distribution is isotropic, where $\lambda_1 = \lambda_2 = \lambda_3 = \frac{1}{3}$, and $\zeta = 1$ if and only if all grains align along one direction, where $\lambda_1 = 1$ and $\lambda_2 = \lambda_3 = 0$.

In Continuum Mechanics [12], the velocity gradient **L**, which is the change of velocity components with respect to position is defined by

$$\mathbf{L} = \text{grad}\, \mathbf{v}\,, \tag{2.7}$$

where **v** is the velocity field. **L** can be decomposed to symmetric and skew-symmetric parts as

$$\mathbf{L} = \mathbf{D} + \mathbf{W} , \tag{2.8}$$

where **D** is the symmetric part of the velocity gradient, which is called the rate of deformation and defined by

$$\mathbf{D} = \frac{1}{2} (\mathbf{L} + \mathbf{L}^{T}) . \tag{2.9}$$

Whereas, **W** is the skew-symmetric part of the velocity gradient, which is called vorticity and is given by

$$\mathbf{W} = \frac{1}{2} (\mathbf{L} - \mathbf{L}^{T}) . \tag{2.10}$$

By taking the material time derivative of **A** in equation (2.2), which is the rate of the change of a quantity **A** in time following the same grains, the following is obtained

$$\dot{\mathbf{A}} = \frac{d}{dt} \oint_{s2} f(\mathbf{k})\, \mathbf{k} \otimes \mathbf{k}\, da . \tag{2.11}$$

Since the integral domain is not changing with time, the differentiation operator can be brought into the integral as

$$\dot{\mathbf{A}} = \oint_{s2} \overline{\dot{f(\mathbf{k})}\, da}\, \mathbf{k} \otimes \mathbf{k} + f(\mathbf{k})\, da\, \overline{\dot{\mathbf{k}} \otimes \mathbf{k}} . \tag{2.12}$$

Since $f(\mathbf{k})\, da$ is constant, the first term in equation (2.12) vanishes and it is simplified to

$$\dot{\mathbf{A}} = \oint_{s2} f(\mathbf{k}) (\dot{\mathbf{k}} \otimes \mathbf{k} + \mathbf{k} \otimes \dot{\mathbf{k}})\, da , \tag{2.13}$$

where $\dot{\mathbf{k}}$ is material time derivative of **k** and it is defined as

$$\dot{\mathbf{k}} = \mathbf{W}\mathbf{k} + \lambda (\mathbf{D}\mathbf{k}) , \tag{2.14}$$

where the parameter λ governs the tendency to align with the rate of deformation **D**. By substituting equation (2.14) into the equation (2.13) and adding a correction term to satisfy the traceless requirement and a relaxation toward isotropic distribution term to consider collisions between grains, it yields the form

$$\dot{\mathbf{A}} = \mathbf{WA} - \mathbf{AW} + \lambda [\, \mathbf{DA} + \mathbf{AD} - 2 (\mathbf{A} \cdot \mathbf{D}) \mathbf{A} \,] - \psi \left\| \mathbf{D}' \right\| (\mathbf{A} - \mathbf{I} / 3) , \tag{2.15}$$

where $\mathbf{D}'$ is deviatoric part of the rate of deformation and defined by

$$\mathbf{D}' = \mathbf{D} - \tfrac{1}{3} \text{ Trace } (\mathbf{D}) \, \mathbf{I} , \tag{2.16}$$

and $\left\| \mathbf{D}' \right\|$ is the magnitude of $\mathbf{D}'$ and defined as

$$\left\| \mathbf{D}' \right\| = \sqrt{\mathbf{D}' \cdot \mathbf{D}'} . \tag{2.17}$$

In this model, there are two model parameters λ, and ψ. The parameter λ is equal to zero for spherical grains and as the grains get more ellipsoidal, $| \lambda |$ increases. The parameter ψ accounts for the collision between grains yielding grains misalignment. It is assumed that the relaxation toward isotropic distribution is proportional to granular temperature, which is usually seen proportional to the shear rate $\| \mathbf{D}' \|$. Although these two parameters can be a function of the shape of grains, size of the grains, pressure, rate of deformation and orientational tensor, as a first approximation, they are considered to be only a function of the shape of grains, which is characterized by r_g defined by

$$r_g = \frac{l - d}{l + d} = \begin{cases} (0,1) & \text{rice} \\ 0 & \text{bead} \\ (-1,0) & \text{lentil} \end{cases} , \tag{2.18}$$

where l and d are geometrical length and width of the grains, respectively. This convenient measurement of the shape ratio is $-1 < r_g < 1$, where r_g is equal to zero for spherical grains,

it is positive and increasing with the elongation of the prolate grains, where l > d, and it is negative and decreasing with the flatness of oblate grains, where d > l.

The parameters λ and ψ are obtained by comparison of the orientational tensor, which is determined by the model for steady-state simple shear and DEM simulation, where determining values for λ and ψ in the model to get the best agreement. The simple shear simulations are performed for different r_g values and the associated λ and ψ are determined, which result in the empirical relations

$$\lambda(r_g) = \frac{2}{\pi} \tan^{-1}(5.5\, r_g), \quad \psi(r_g) = 0.85 \exp(-4\, r_g^2), \tag{2.19}$$

where these functional forms are obtained by curve fitting. They are based on data in the range $r_g \in [-0.6, -0.2]$ and $r_g \in [0.2, 0.7]$ and might not be accurate for the smaller or larger values of $|r_g|$.

Equation (2.15) is used as a governing equation and it is solved in the domain numerically using MATLAB. In this project, dimensions of various grains such as rice and lentil are provided by experiment to determine r_g values for rice and lentils as

Material	Minor Axis	Major Axis	r_g
Jasmine Rice	1.5	6.7	0.63
Red Lentils	1.6	4.5	– 0.48

Table 1 : Properties of grains used in the experimental setup

2-2 Discretization

The geometry is a rectangular hopper similar to [1]. The hopper has a rectangle opening with a fixed dimension the same as the width of the hopper and the other variable dimension including 10 mm and 15 mm that is along with the length of the hopper. The coordinate plane is organized around two axes. The x-axis runs horizontally along the length of the hopper and the y-axis runs vertically along the height of the hopper. The coordinate system origin is placed at the top left corner of the x and y plane of the hopper. The z-axis runs along with the width of the hopper. The geometry is meshed with 119 nodes in the y-axis and 78 nodes in the x-axis where there is an equal distance of 1.712 mm between the nodes in the x-axis and y-axis. The nodes in the y-axis are identified by i, which increases downward y_i and the nodes in the x-axis are identified by j, which increases toward the right x_j. The center of the opening is placed in the middle of the length of the hopper.

Position of grains in the hopper and the velocity field are provided by experiments. The velocity field was defined in 2-D, since the velocity in z-axis was negligible in comparison to the plane velocity. The numerical analysis is performed to the center of the domain including 106 nodes in the height of the hopper from 5 to 110 node and 21 nodes in the length of hopper from 30 to 50 node to avoid the stagnation zones, where there is not a significant flow which is required for the model to predict the orientation field of grains.

The velocity field is defined as

$$\mathbf{v} = u\ \hat{\mathbf{i}} + v\ \hat{\mathbf{j}} + w\ \hat{\mathbf{k}}\,, \tag{2.20}$$

where u is the velocity component in the x-direction, v is the velocity component in the y-direction, and w is the velocity component in the z-direction. To discretize the governing equation (2.15), it should be noted that

$$\dot{\mathbf{A}} = \frac{\partial \mathbf{A}}{\partial T} + (\text{grad}\ \mathbf{A})\,\mathbf{v} = \frac{\partial \mathbf{A}}{\partial T} + u\frac{\partial \mathbf{A}}{\partial x} + v\frac{\partial \mathbf{A}}{\partial y} + w\frac{\partial \mathbf{A}}{\partial z}\,, \tag{2.21}$$

where grad **A** is the gradient of **A** with respect to the position. Since it is steady-state and the velocity component in the z-direction vanishes, equation (2.21) is simplified to

$$\dot{\mathbf{A}} = u\frac{\partial \mathbf{A}}{\partial x} + v\frac{\partial \mathbf{A}}{\partial y}. \tag{2.22}$$

By substitution of equation (2.22) in the governing equation (2.15), it is simplified to

$$u\frac{\partial \mathbf{A}}{\partial x} + v\frac{\partial \mathbf{A}}{\partial y} = \mathbf{WA} - \mathbf{AW} + \lambda\,[\,\mathbf{DA} + \mathbf{AD} - 2\,(\,\mathbf{A}\cdot\mathbf{D}\,)\,\mathbf{A}\,] - \psi\,\|\mathbf{D}'\|\,(\mathbf{A} - \mathbf{I}/3). \tag{2.23}$$

Since $\frac{\partial \mathbf{A}}{\partial x}$ is the change of **A** with respect to the position horizontally and $\frac{\partial \mathbf{A}}{\partial y}$ is the change of **A** with respect to the position vertically which contains the evolution of **A** in the height of the hopper as the grains flow down, equation (2.23) is solved for $\frac{\partial \mathbf{A}}{\partial y}$ and discretized in the domain where $\square_{i,j} = \square|_{y_i, x_j}$ as

$$\left(\frac{\partial \mathbf{A}}{\partial y}\right)_{i,j} = \left(\left(\mathbf{W}_{i,j}\,\mathbf{A}_{i,j} - \mathbf{A}_{i,j}\,\mathbf{W}_{i,j} + \lambda\left[\mathbf{D}_{i,j}\,\mathbf{A}_{i,j} + \mathbf{A}_{i,j}\,\mathbf{D}_{i,j} - 2\left(\mathbf{A}_{i,j}\cdot\mathbf{D}_{i,j}\right)\mathbf{A}_{i,j}\right] - \psi\,\|\mathbf{D}'_{i,j}\|\left(\mathbf{A}_{i,j} - \frac{\mathbf{I}}{3}\right)\right) - u_{i,j}\left(\frac{\partial \mathbf{A}}{\partial x}\right)_{i,j}\right) v_{i,j}^{-1}, \tag{2.24}$$

where $\left(\frac{\partial \mathbf{A}}{\partial x}\right)_{i,j}$ is approximated by the second order accuracy of finite difference formulations including central difference, forward difference, and backward difference that

are mentioned in detail in the appendix and $\left(\frac{\partial \mathbf{A}}{\partial y} \right)_{i,j}$ is approximated by the first order accuracy of finite difference formulation as

$$\left(\frac{\partial \mathbf{A}}{\partial y} \right)_{i,j} = (\mathbf{A}_{i+1,j} - \mathbf{A}_{i,j}) (\Delta y)^{-1} , \tag{2.25}$$

where $\mathbf{A}_{i+1,j}$ is the predicted orientational tensor for the next position downstream. By substitution of equation (2.25) in equation (2.24) and solving for $\mathbf{A}_{i+1,j}$, the discretized governing equation is simplified to

$$\mathbf{A}_{i+1,j} = \mathbf{A}_{i,j} +$$

$$\left(\left(\mathbf{W}_{i,j} \mathbf{A}_{i,j} - \mathbf{A}_{i,j} \mathbf{W}_{i,j} + \lambda \left[\mathbf{D}_{i,j} \mathbf{A}_{i,j} + \mathbf{A}_{i,j} \mathbf{D}_{i,j} - 2 \left(\mathbf{A}_{i,j} \cdot \mathbf{D}_{i,j} \right) \mathbf{A}_{i,j} \right] - \psi \left\| \mathbf{D}'_{i,j} \right\| \left(\mathbf{A}_{i,j} - \frac{\mathbf{I}}{3} \right) \right) -$$

$$u_{i,j} \left(\frac{\partial \mathbf{A}}{\partial x} \right)_{i,j} \Bigg) v_{i,j}^{-1} \Delta y . \tag{2.26}$$

The discretized velocity field is defined as

$$\mathbf{v}_{i,j} = u_{i,j} \, \hat{\mathbf{i}} + v_{i,j} \, \hat{\mathbf{j}} + w_{i,j} \, \hat{\mathbf{k}} , \tag{2.27}$$

where $\mathbf{v}_{i,j}$ is defined in 3-D and the velocity gradient is defined as

$$[\mathbf{L}_{i,j}] = \begin{bmatrix} \partial u_{i,j} / \partial x & \partial u_{i,j} / \partial y & \partial u_{i,j} / \partial z \\ \partial v_{i,j} / \partial x & \partial v_{i,j} / \partial y & \partial v_{i,j} / \partial z \\ \partial w_{i,j} / \partial x & \partial w_{i,j} / \partial y & \partial w_{i,j} / \partial z \end{bmatrix} . \tag{2.28}$$

The discretized rate of deformation $\mathbf{D}_{i,j}$ is defined as

$$[\mathbf{D}_{i,j}] = \begin{bmatrix} \partial u_{i,j}/\partial x & \frac{1}{2}\left(\partial u_{i,j}/\partial y + \partial v_{i,j}/\partial x\right) & \frac{1}{2}\left(\partial u_{i,j}/\partial z + \partial w_{i,j}/\partial x\right) \\ \frac{1}{2}\left(\partial v_{i,j}/\partial x + \partial u_{i,j}/\partial y\right) & \partial u_{i,j}/\partial y & \frac{1}{2}\left(\partial v_{i,j}/\partial z + \partial w_{i,j}/\partial y\right) \\ \frac{1}{2}\left(\partial w_{i,j}/\partial x + \partial u_{i,j}/\partial z\right) & \frac{1}{2}\left(\partial w_{i,j}/\partial y + \partial v_{i,j}/\partial z\right) & \partial w_{i,j}/\partial z \end{bmatrix}, \quad (2.29)$$

and the discretized vorticity $\mathbf{W}_{i,j}$ as

$$[\mathbf{W}_{i,j}] = \begin{bmatrix} 0 & \frac{1}{2}\left(\partial u_{i,j}/\partial y - \partial v_{i,j}/\partial x\right) & \frac{1}{2}\left(\partial u_{i,j}/\partial z - \partial w_{i,j}/\partial x\right) \\ -\frac{1}{2}\left(\partial u_{i,j}/\partial y - \partial v_{i,j}/\partial x\right) & 0 & \frac{1}{2}\left(\partial v_{i,j}/\partial z - \partial w_{i,j}/\partial y\right) \\ -\frac{1}{2}\left(\partial u_{i,j}/\partial z - \partial w_{i,j}/\partial x\right) & -\frac{1}{2}\left(\partial v_{i,j}/\partial z - \partial w_{i,j}/\partial y\right) & 0 \end{bmatrix}. \quad (2.30)$$

It should be noted that since the velocity component in the z-direction is negligible in comparison to the plane velocity components and the velocity variation in the z-direction is very small, $w_{i,j} = 0$ and $\partial/\partial z = 0$.

The second order accuracy of finite difference formulations are used to approximate $\mathbf{D}_{i,j}$ and $\mathbf{W}_{i,j}$ in the domain.

2-3 Numerical Results

2-3-1 Initial Condition

For solving the ordinary differential equations (2.26), an initial condition must be specified. Since, we decide to compare the model results to the experimental measurements, we adopt the same condition as the experiment. Therefore, the orientation field of grains at the highest layer of the hopper is considered to be the x-z plane isotropy. In the experiment, the x and y plane orientation field of grains is measured. Whereas, in the numerical calculation, the model predicts the orientation field of grains in 3-D. To project the orientation field in the z-direction to the plane orientation field, the orientation field in the z-direction is taken and add half of this amount fairly to the orientation field in x and y directions.

The governing equation (2.15) is a first order ordinary differential equation, which does not require boundary conditions to be solved.

2-3-2 Visualization of Orientation Distribution of Grains

The orientation field is determined by applying equation (2.26) in the domain. An ellipsoidal shape is used to visualize the orientation field of grains in the domain. It is considered the larger eigenvalue as the longer dimension of the ellipsoidal shape and the smaller eigenvalue as the shorter dimension of the ellipsoidal shape as it is shown in figure (1). The geometry of the ellipses represents the eigenvalues and the orientation field of grains. The associated eigenvector to the larger eigenvalue is considered for orientation angle and it is defined as

$$\theta = \tan^{-1}\left(\frac{e_1{}^{y}}{e_1{}^{x}}\right), \tag{2.31}$$

where $e_1{}^{y}$ is the $\mathbf{e}_1$ component in y-direction and $e_1{}^{x}$ is the $\mathbf{e}_1$ component in x-direction.

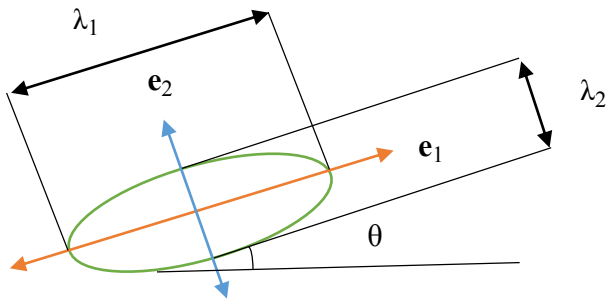

Figure 1 : Visualization of the orientation distribution

2-3-3 Analyzed Domain

The analyzed domain is considered 80 mm below the highest layer of the domain and 3 mm above the opening (from 80 mm to 188 mm in the y-direction and from 39 mm to 74 mm in the x-direction) to show the orientation field better.

The experimental data is available from 7 mm to 191 mm in the y-direction and from 10 mm to 108 mm in the x-direction. Whereas, the numerical analysis is performed from 7 mm to 188 mm in the y-direction and from 39 mm to 74 mm in the x-direction to neglect stagnation zones. The center of the opening is placed at zero, where it is high lighted.

The detailed information regarding the streamlines and velocity field are provided in [1].

2-3-4 Rice

Figures 2 and 3 show the orientation field of rice in the analyzed domain in the hopper with 10 mm and 15 mm openings, respectively. It is observed that rice orient with the streamline at farther upstream for the smaller opening in comparison to the larger opening. It is observed that rice for both cases of opening size is more sphere in the center in comparison to the edges of the analyzed domain, which means rice is less aligned with respect to each other for each position in the center in comparison to the edges of the analyzed domain.

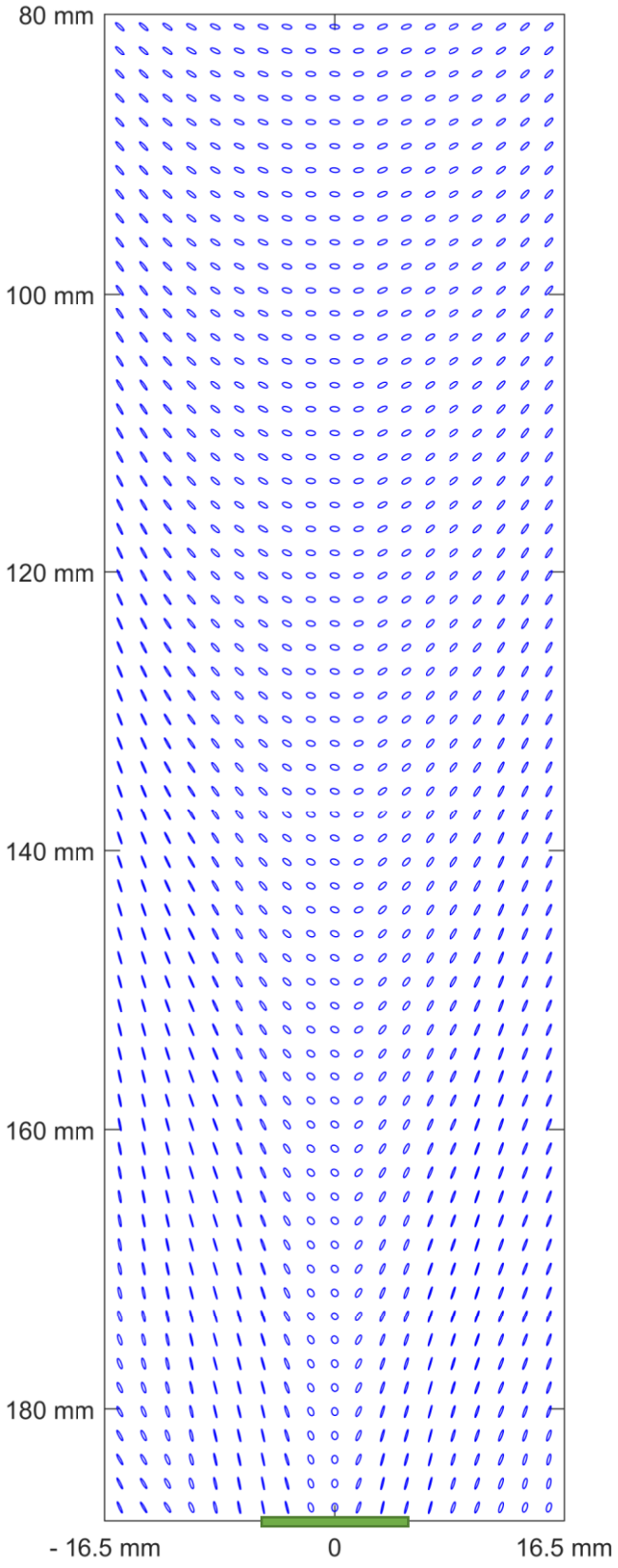

Figure 2 : Orientation field of rice in hopper flow (opening 10 mm)

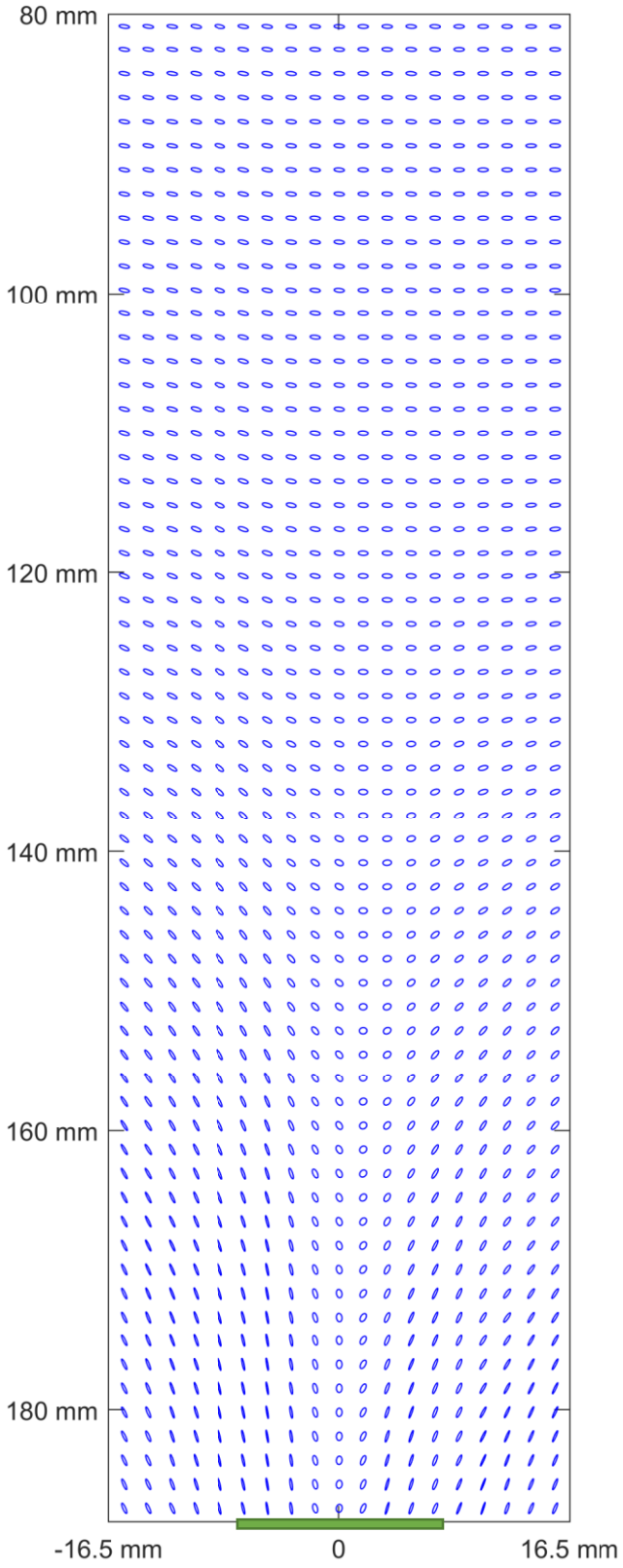

Figure 3 : Orientation field of rice in hopper flow (opening 15 mm)

2-3-5 Lentil

Figures 4 and 5 show the orientation field of lentils in the analyzed domain in the hopper with 10 mm and 15 mm openings, respectively. Lentil has different λ and ψ including a negative value for λ and a different positive value for ψ compared to rice due to having different r_g. Similar to rice, it is observed that lentils orient with the streamline at farther upstream for the smaller opening in comparison to the larger opening. However, rice orient with the streamline at farther upstream in comparison to lentils for the smaller opening which this can be rooted that rice has more ellipsoidal shape compared to lentil. It is observed that lentils for both cases of opening size are more sphere in the center in comparison to the edges of the analyzed domain, which means lentils are less aligned with respect to each other for each position in the center in comparison to the edges of the analyzed domain.

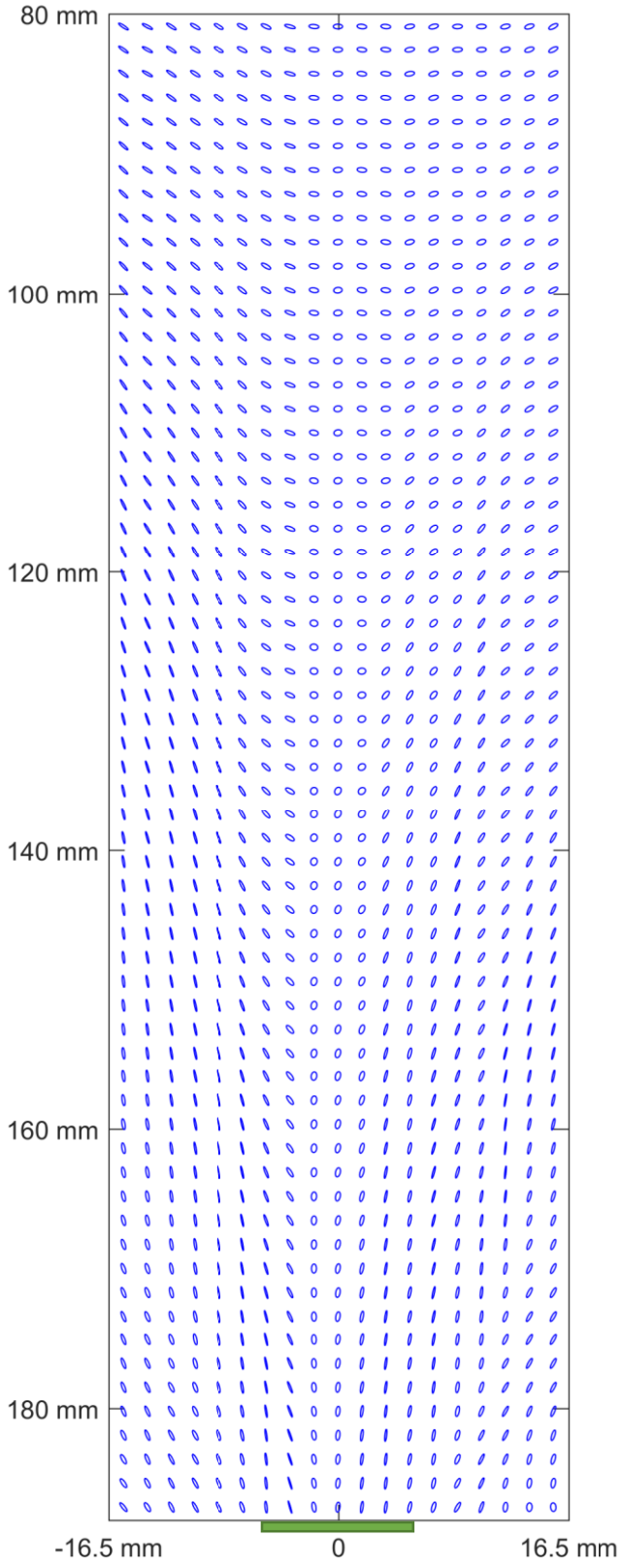

Figure 4 : Orientation field of lentil in hopper flow (opening 10 mm)

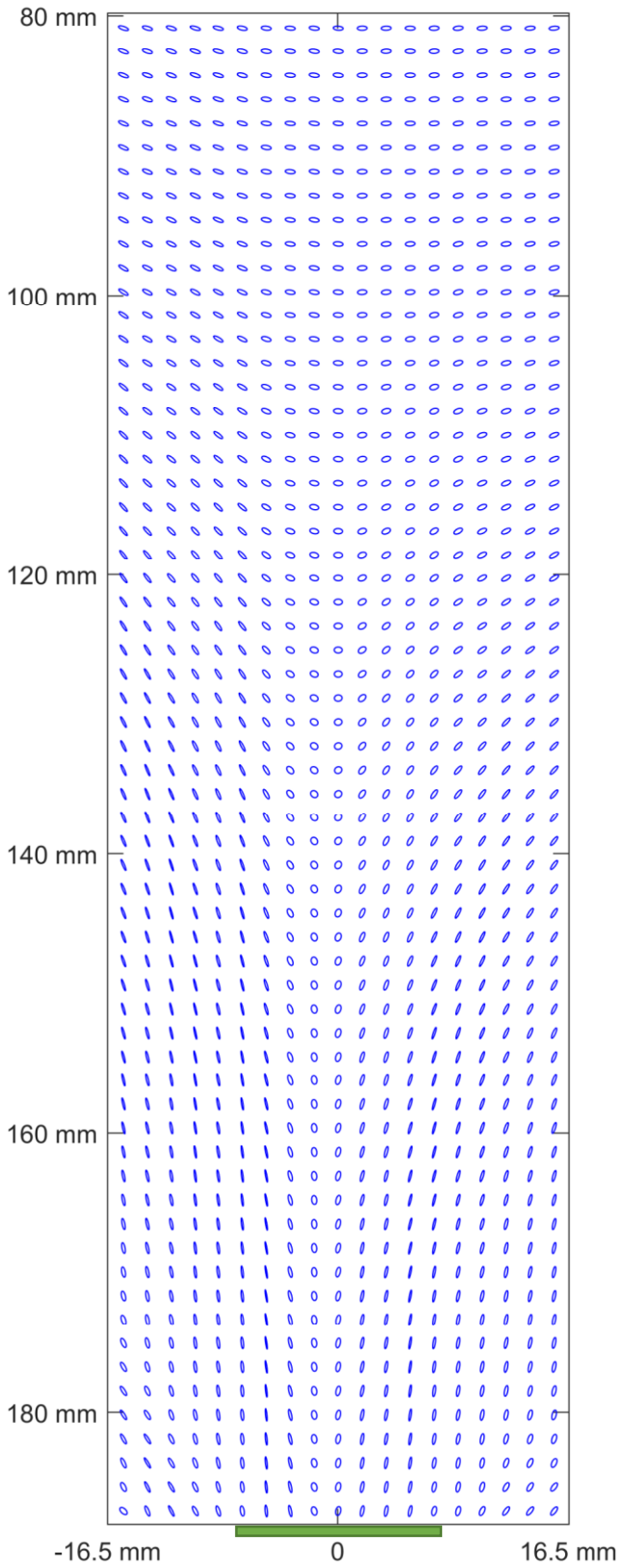

Figure 5 : Orientation field of lentil in hopper flow (opening 15 mm)

Chapter 3 : Model and Experimental Comparison

The results obtained by solving the model in the domain are compared with the experimental measurements. Linear interpolation is performed to the experimental data to have similar nodes with the model results. The experimental data is visualized Similarly to the model by ellipsoidal shapes for comparison.

The goal of this project is to investigate the performance of the model in complex flow fields such as hopper flows. The main focus is on the qualitative agreement between the model predictions and the experiments. Since the experimental data contains large variations in both the measured velocity filed and orientation of grains, the quantitative comparison might not be appropriated. However, a quantitative comparison can be represented by the orientation tensor error measured as

$$E_{\mathbf{A}} = \frac{1}{2226} \sum_{i=5}^{110} \sum_{j=30}^{50} \frac{\| \mathbf{A}_{i,j}^{exp} - \mathbf{A}_{i,j}^{mod} \|}{\| \mathbf{A}_{i,j}^{exp} \|} \quad , \tag{3.1}$$

where $\mathbf{A}_{i,j}^{exp}$ is the experimental orientational tensor and $\mathbf{A}_{i,j}^{mod}$ is the model orientational tensor at each node. The results are shown in table (1).

Grains	Rice		Lentil	
Opening	10 mm	15 mm	10 mm	15 mm
$E_{\mathbf{A}}$	0.9110	0.8993	0.9344	0.9249

Table 2 : Comparison between the experimental and model orientation field of grains

Since the worst case scenario for E_A is 1 where for example, the orientation field of grains obtained by the model is horizontal and the orientation field obtained by the experimental measurements is vertical, the values of E_A in the table (1) is large.

In [1], figure 7 represents the uncertainty of the experimental measurements, which the interval is showed by the shaded area with the 95% confidence interval on the estimated mean orientation angle. The numerical uncertainty is measured on the mean orientation angle in the domain with 95% confidence interval of 34.2831 ± 29.549 degrees for rice and 34.4814 ± 31.8958 degrees for lentils.

3-1 Rice Orientation Distribution Comparison

Figures 6 and 7 show the orientation field comparison for rice between the model calculations and experimental measurements in the analyzed domain in the hopper with 10 mm and 15 mm openings, respectively. The red ellipsoidal shapes are used to visualize the experimental data and the blue ones are used to visualize the model orientation field. It is observed that the orientation field of rice obtained by the model matches better to the experimental measurements in the center in comparison to the edges of the analyzed domain. This indicates that the model predicts the orientation field better, where there is a significant flow.

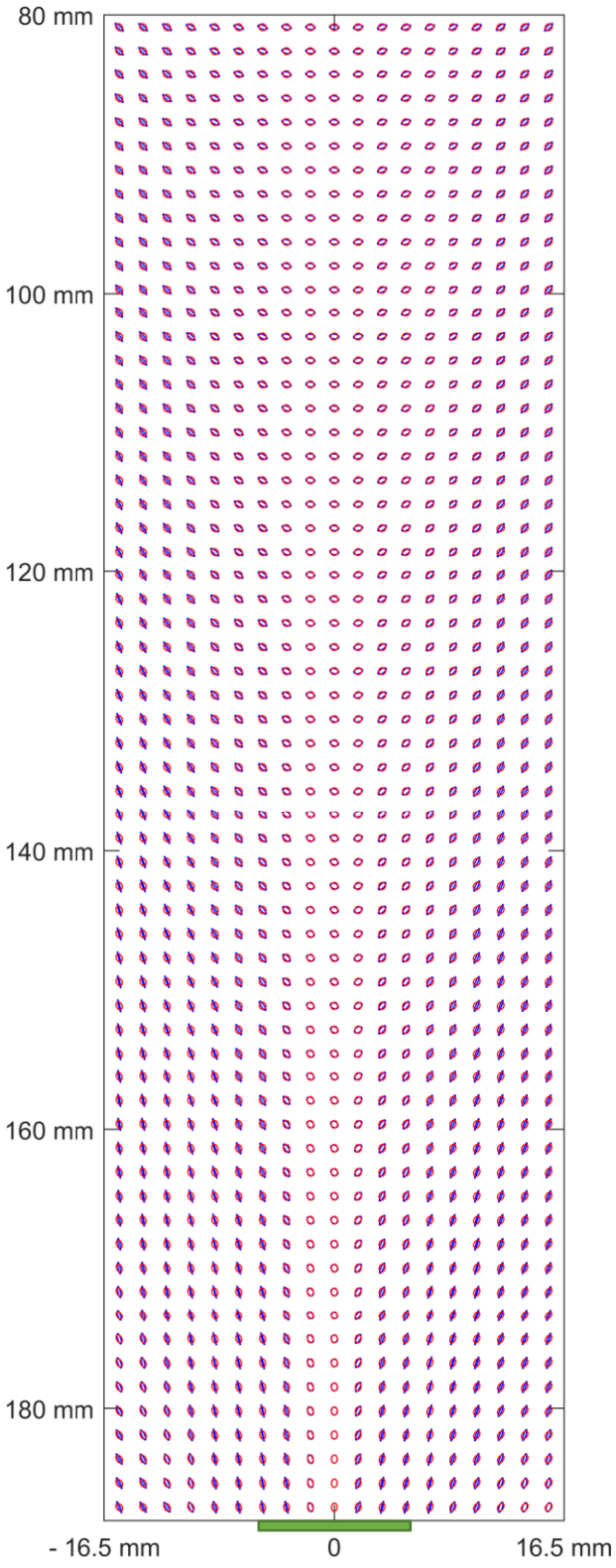

Figure 6 : Model and experimental comparison of the orientation field for rice (opening 10 mm). Blue ellipsoidal shapes are obtained from the model and the red ellipsoidal shapes are taken from the experimental measurements.

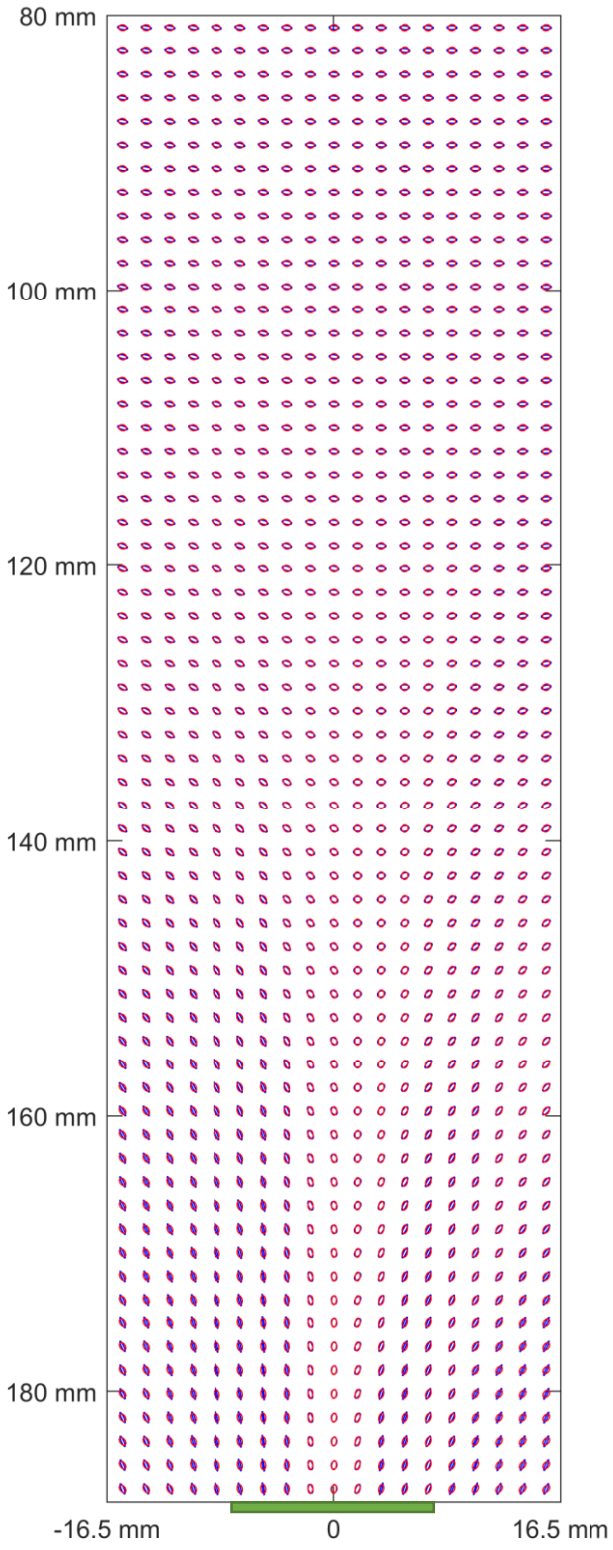

Figure 7 : Model and experimental comparison of the orientation field for rice (opening 15 mm). Blue ellipsoidal shapes are obtained from the model and the red ellipsoidal shapes are taken from the experimental measurements.

3-2 Lentil Orientation Distribution Comparison

Figures 8 and 9 show orientation field comparison for lentils between the model calculations and experimental measurements in the analyzed domain in the hopper with 10 mm and 15 mm openings, respectively. The red ellipsoidal shapes are used to visualize the experimental data and the blue ones are used to visualize the model orientation field. Similar to rice, it is observed that the orientation field for lentils obtained by the model matches better to the experimental measurements in the center in comparison to the edges of the analyzed domain.

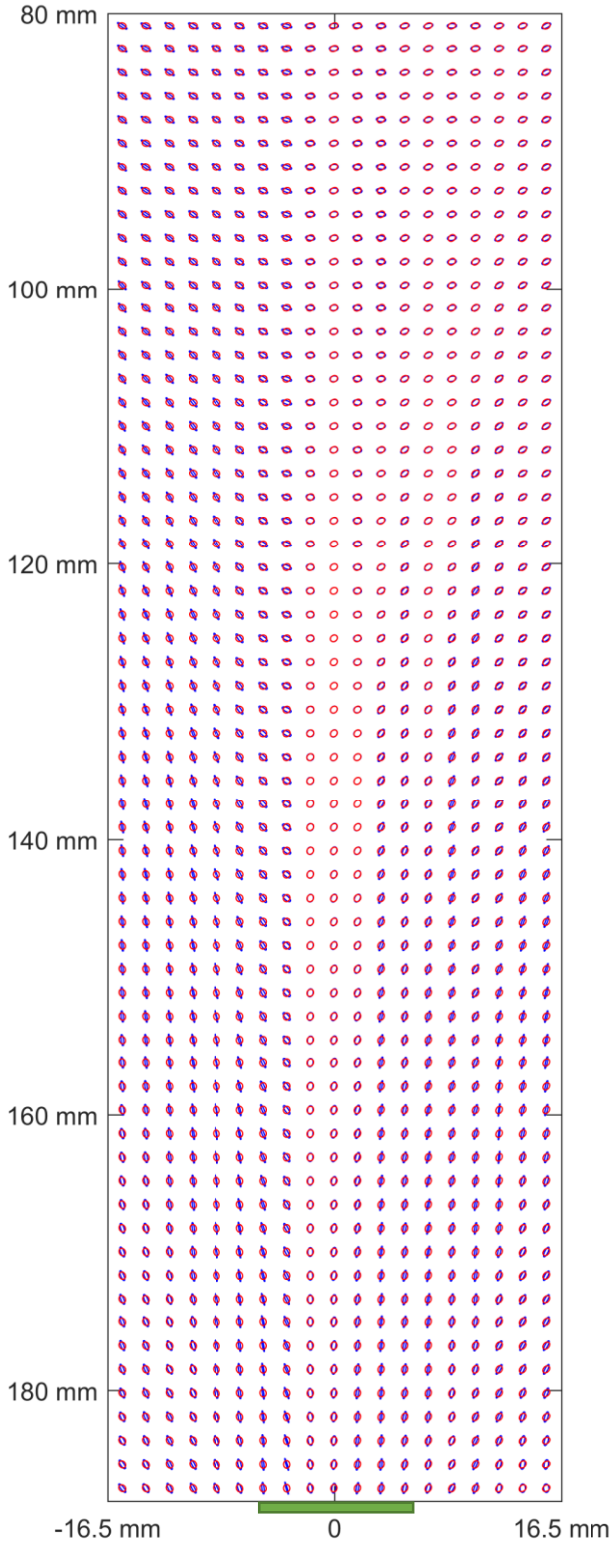

Figure 8 : Model and experimental comparison of the orientation field for lentil (opening 10 mm). Blue ellipsoidal shapes are obtained from the model and the red ellipsoidal shapes are taken from the experimental measurements.

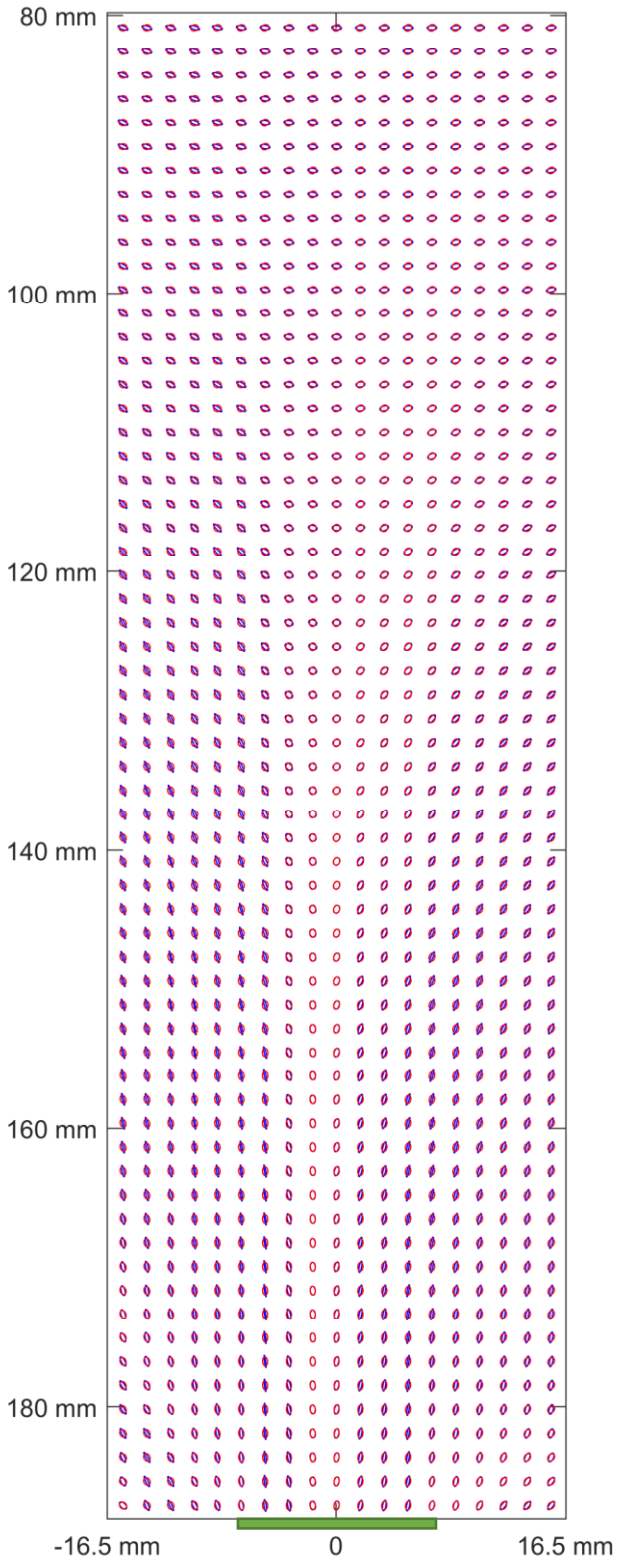

Figure 9 : Model and experimental comparison of the orientation field for lentil (opening 15 mm). Blue ellipsoidal shapes are obtained from the model and the red ellipsoidal shapes are taken from the experimental measurements.

3-3 Principal Average Orientational Angle Comparison

The average principal orientational angle is measured by considering only in the center of the domain from nodes 37 to 41 in the x-direction and from nodes 5 to 110 in the y-direction, where node 5 has the height of 0.7 cm and node 110 has the height of 18.7 cm as the following. This area is selected to consider on the part of the domain, where there is a significant flow. It is defined as

$$\theta_{ave} = \frac{1}{530} \sum_{i=5}^{110} \sum_{j=37}^{41} \tan^{-1}(\theta_{ij}), \tag{3.2}$$

Figures 10 and 11 show the principal average orientational angle for rice and lentil per height of the hopper. The average model principal orientation of rice and lentils are horizontal, where the grains lie horizontally at the highest layer of the domain and it changes to vertical, where the grains get closer to the opening. The model principal average orientational angle agrees with the experimental measurements as it is shown in the following figures.

This comparison indicates that the model is able to estimate the average orientation of grains at any position in space and time even smoother than by the experiment method.

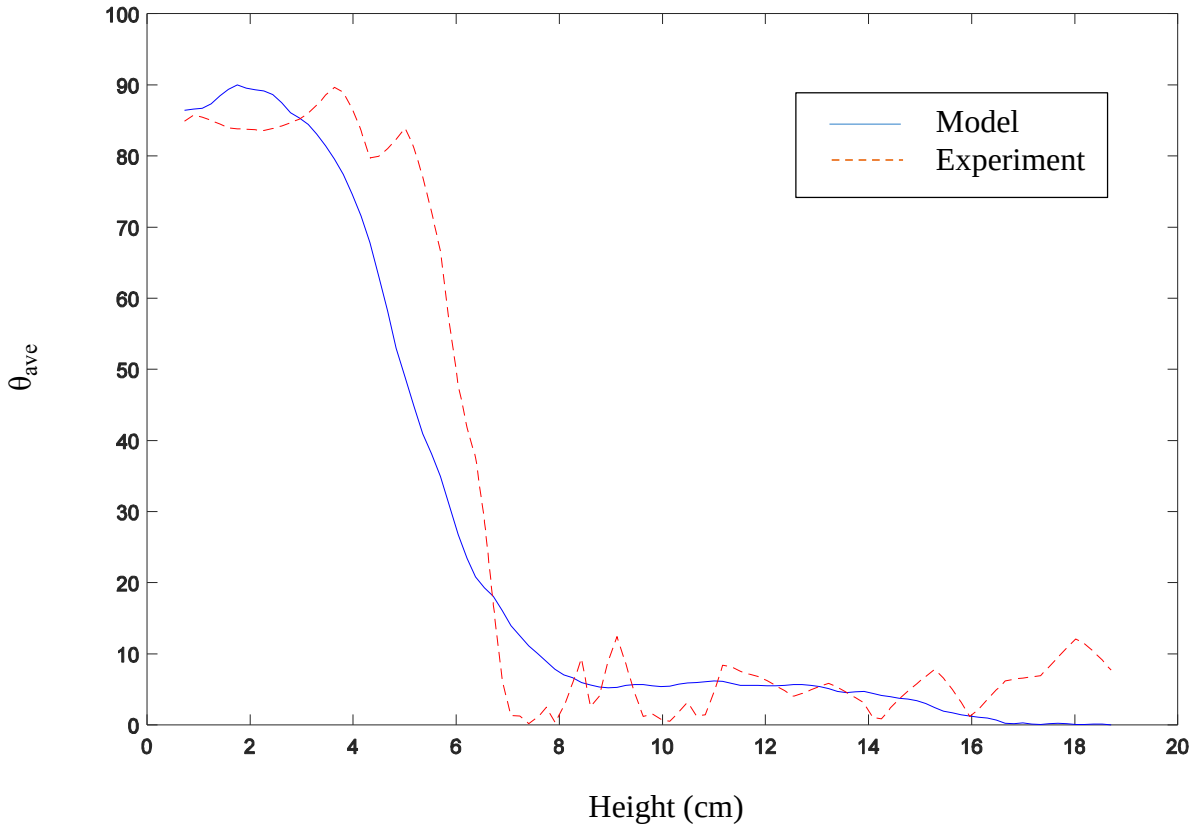

Figure 10 : Model and experimental comparison of the average principal orientational angle per height of the hopper for rice. The blue curve is from the model and the red dashed curve is from the experiment measurements.

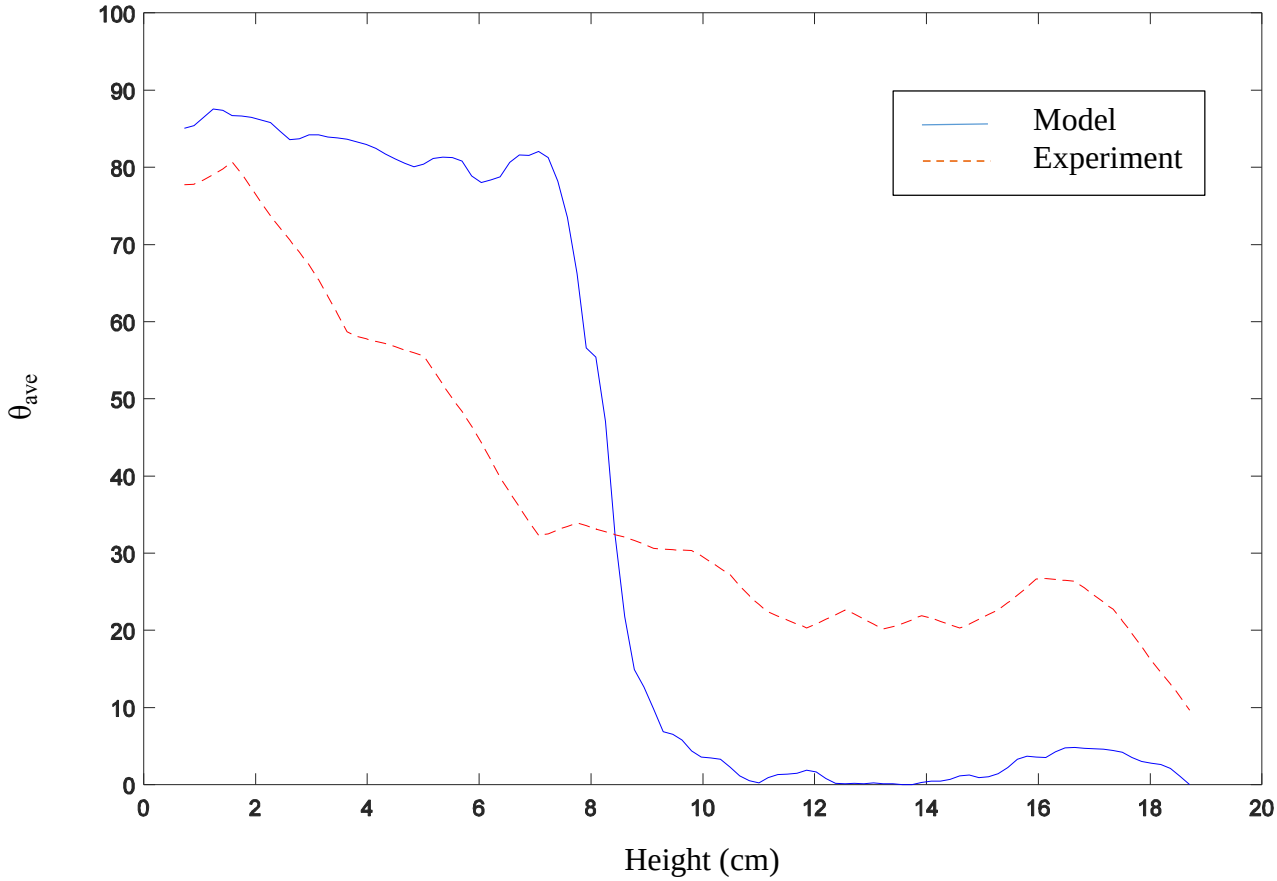

Figure 11 : Model and experimental comparison of the average principal orientational angle per height of the hopper for lentil. The blue curve is from the model and the red dashed curve is from the experiment measurements.

Chapter 4 : Determination of The Model Parameters

The parameters λ and ψ that depend on the shape of grains are determined to have a better agreement between the model calculations and experimental measurements. The "fminsearch" function in MATLAB [14] is used to minimize the orientation angle between the model and the experimental measurements that is called orientation angle error ($\min_{\lambda,\psi} e_\theta$)

$$E_\theta = \frac{1}{2226} \sum_{i=5}^{110} \sum_{j=30}^{50} | \theta_{i,j}^{exp} - \theta_{i,j}^{mod} | , \quad (4.1)$$

where $\theta_{i,j}^{exp}$ contains the experiment orientational angle and $\theta_{i,j}^{mod}$ contains the model orientational angle at each node. Since $\mathbf{A}_{i,j}^{exp}$ considered only on the plane orientation distribution of the grains, whereas $\mathbf{A}_{i,j}^{mod}$ considered on the orientation distribution of grains in 3-D at each node, the plane orientational angle is considered for the comparison between the model results and experimental measurements to determine the model parameters.

figures 12, 13, 14, and 15 show the orientation field comparison between the experimental measurements and model calculations with the optimized λ and ψ for rice and lentils in the analyzed domain in the hopper with 10 mm and 15 mm openings. The red ellipsoidal shapes are used to visualize the experimental data and the blue ones are used to visualize the model orientation field. It is observed that the model and experimental orientation field match very well in a way that one color is seen in most positions.

The determined λ and ψ values for rice and lentil in the hopper with 10 mm and 15 mm opening sizes are shown in the table (2).

Orifice Size (mm)	Improved Model Parameters for Rice		Improved Model Parameters for Lentil	
Model Parameters	λ	ψ	λ	ψ
10	0.4690	1.5666	– 0.3423	2.1213
15	0.4582	2.1516	– 0.1423	2.5641
Model Parameters Proposed in [1]	0.8222	0.1701	– 0.7675	0.3442

Table 3 : Determination of model parameters for rice and lentil in the hopper with 10 mm or 15 mm openings.

As it is expected, the parameter λ is a negative number for lentil due to having different r_g compared to rice. The improved model parameters show that there is a huge difference between λ and ψ in comparison to the parameters proposed in [1]. This can be rooted in various aspects such as the error of the experimental measurements and comparing only the plane orientation field. However, $|\lambda|$ is larger for rice compared to lentils since rice has a more ellipsoidal shape and this leads to more alignment.

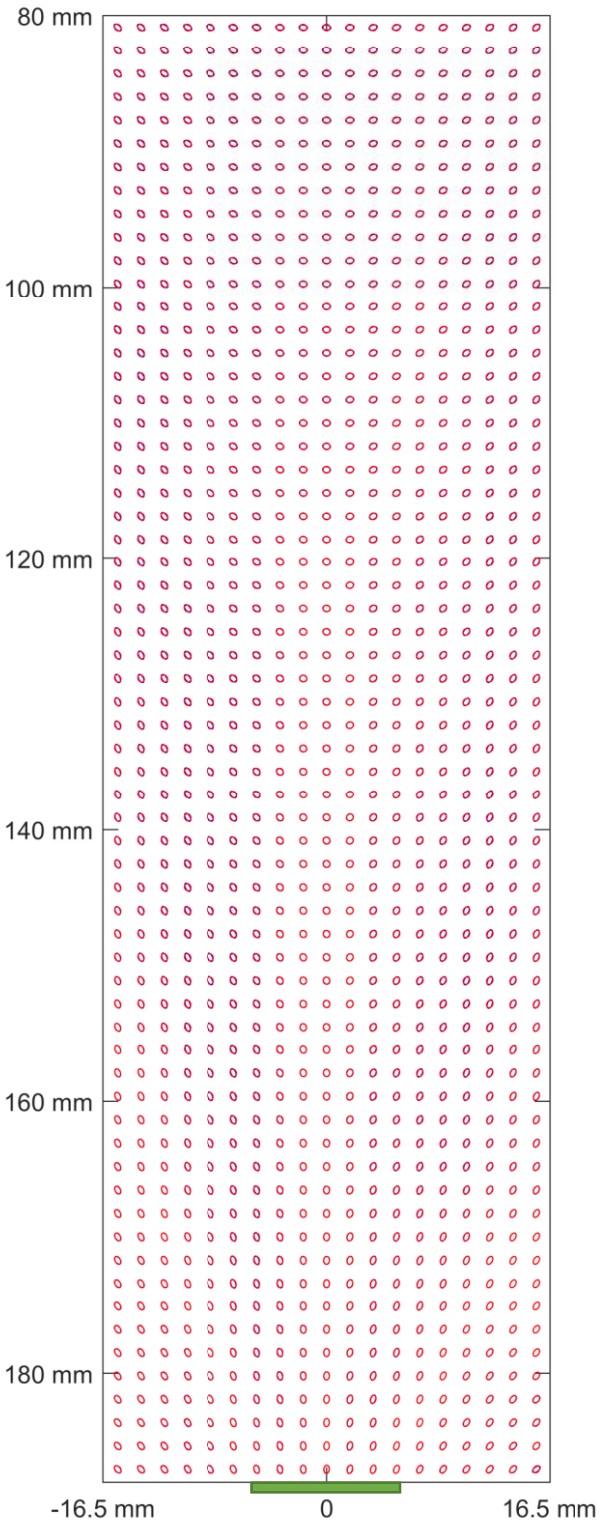

Figure 12 : Model and experimental comparison of the orientation field for rice with the optimized model parameters (opening 10 mm). Blue ellipsoidal shapes are obtained from the model and the red ellipsoidal shapes are taken from the experimental measurements.

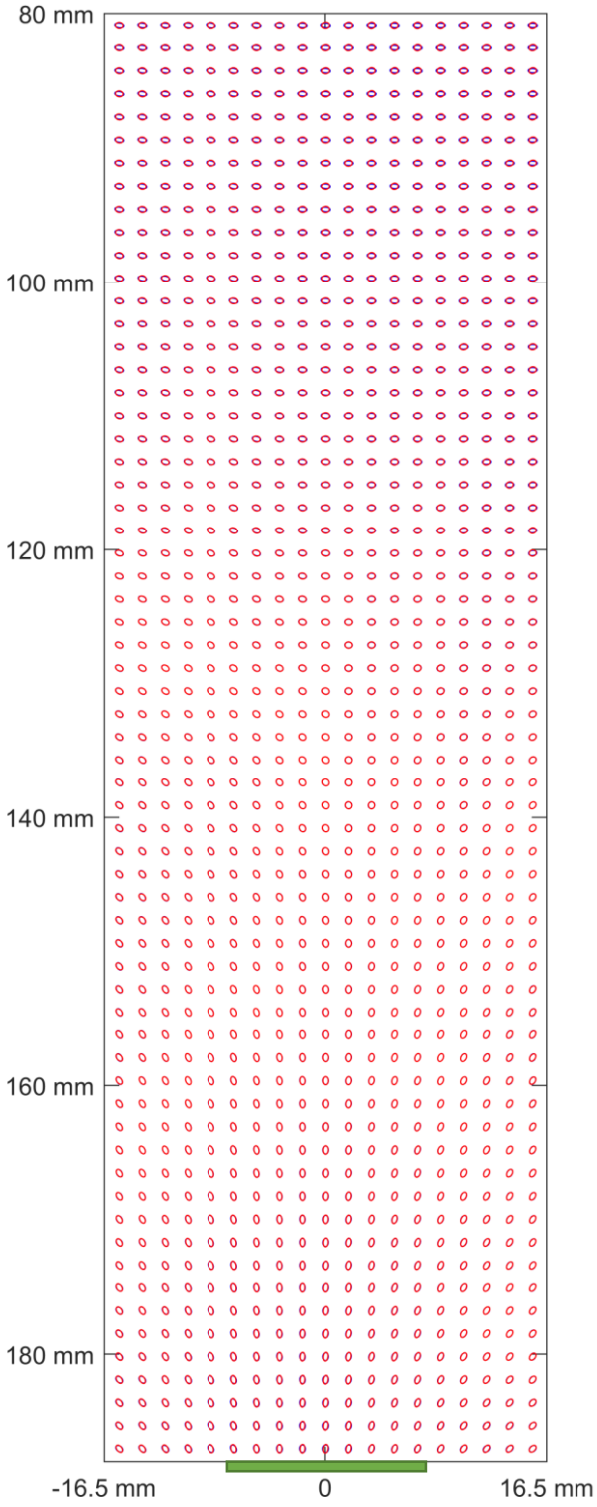

Figure 13 : Model and experimental comparison of the orientation field for rice with the optimized model parameters (opening 15 mm). Blue ellipsoidal shapes are obtained from the model and the red ellipsoidal shapes are taken from the experimental measurements.

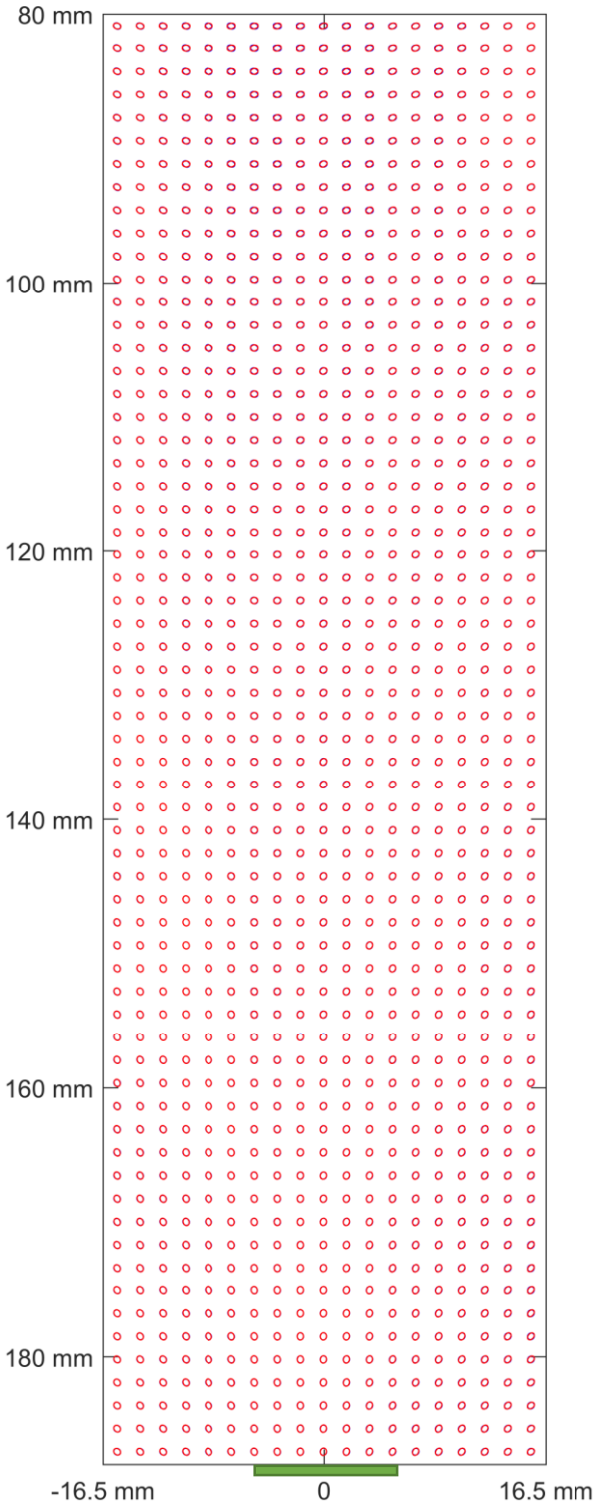

Figure 14 : Model and experimental comparison of the orientation field for lentil with the optimized model parameters (opening 10 mm). Blue ellipsoidal shapes are obtained from the model and the red ellipsoidal shapes are taken from the experimental measurements.

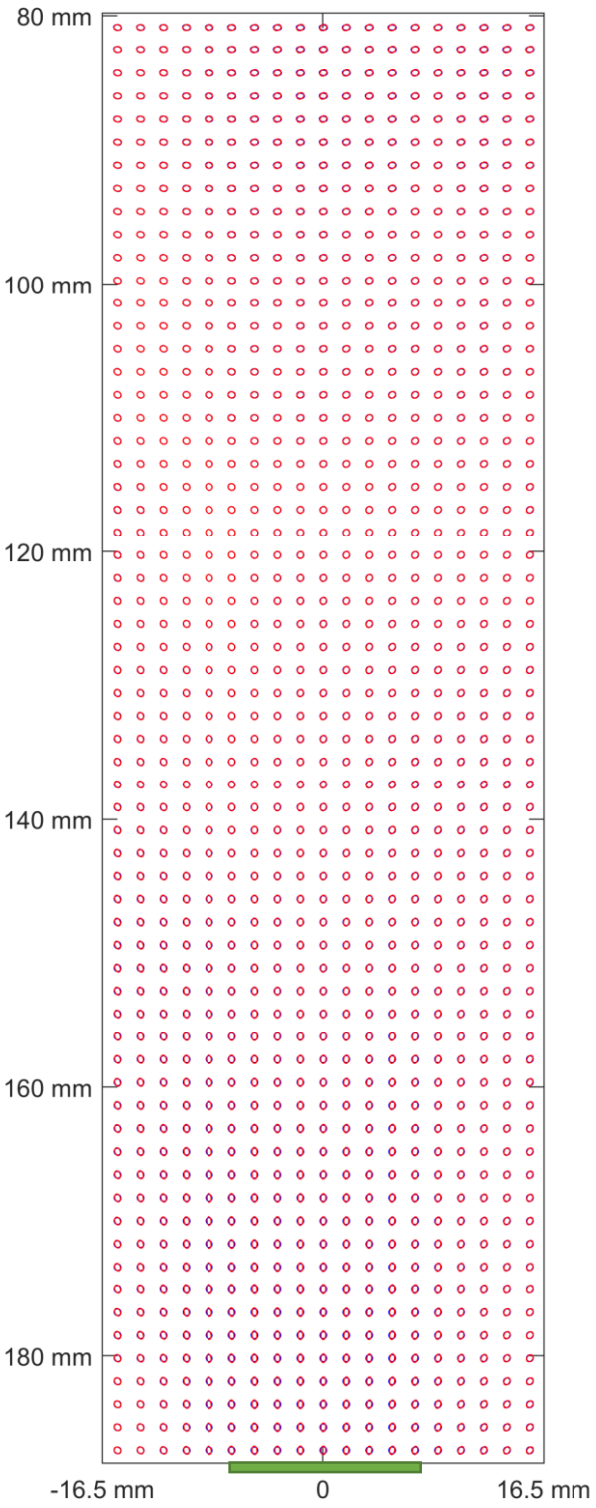

Figure 15 : Model and experimental comparison of the orientation field for lentil with the optimized model parameters (opening 15 mm). Blue ellipsoidal shapes are obtained from the model and the red ellipsoidal shapes are taken from the experimental measurements.

Chapter 5 : Conclusions

The model predicts that rice and lentils orient from horizontal to vertical, as the grains flow down in the domain, which agrees with the experimental measurements. In addition, the orientation field of grains predicted by the model matches with the experimental measurements, where it matches better in the center in comparison to the edges of the analyzed domain of the hopper. The grains orient and align with the streamline at farther upstream in the smaller opening in comparison to the larger opening, which agrees with the experimental measurements.

It can be concluded that the kinematic continuum model is able to well predict the orientation field of grains in the hopper flows since it shows good agreement with the experiment.

Bibliography

[1] F. Guillard, B. Marks, and I. Einav, “Dynamic X-ray radiography reveals particle size and shape orientation fields during granular flow,” Sci. Rep., vol. 7, no. 1, pp. 1–11, 2017.

[2] T. Börzsönyi et al., “Packing, alignment and flow of shape-anisotropic grains in a 3D silo experiment,” New J. Phys., vol. 18, no. 9, 2016.

[3] E. Azéma, I. Preechawuttipong, and F. Radjai, “Binary mixtures of disks and elongated particles: Texture and mechanical properties,” Phys. Rev. E, vol. 94, no. 4, pp. 1–12, 2016.

[4] J. Katagiri, T. Matsushima, and Y. Yamada, “Simple shear simulation of 3D irregularly-shaped particles by image-based DEM,” Granul. Matter, vol. 12, no. 5, pp. 491–497, 2010.

[5] I. Zuriguel, A. Garcimartín, D. Maza, L. A. Pugnaloni, and J. M. Pastor, “Jamming during the discharge of granular matter from a silo,” Phys. Rev. E - Stat. Nonlinear, Soft Matter Phys., vol. 71, no. 5, 2005.

[6] K. To, P. Y. Lai, and H. K. Pak, “Jamming of granular flow in a two-dimensional hopper,” Phys. Rev. Lett., vol. 86, no. 1, pp. 71–74, 2001.

[7] B. Nadler, F. Guillard, and I. Einav, “Kinematic Model of Transient Shape-Induced Anisotropy in Dense Granular Flow,” Phys. Rev. Lett., vol. 120, no. 19, 2018.

[8] E. T. Bowman, K. Soga, and W. Drummond, “Particle shape characterisation using Fourier descriptor analysis,” Géotechnique, vol. 51, no. 6, pp. 545–554, 2004.

[9] R. Kawamoto, J. Andrade, and T. Matsushima, “A 3-D mechanics-based particle shape index for granular materials,” Mech. Res. Commun., vol. 92, no. July, pp. 67–73, 2018.

[10] G. Mollon and J. Zhao, “Advances in realistic generation of grain shapes,” vol. 14, no. 1, p. 69621, 2013.

[11] M. Revay, D. A. H. Hanaor, D. W. Airey, Y. Gan, and I. Einav, “3D printable geomaterials,” Géotechnique, vol. 66, no. 4, pp. 323–332, 2015.

[12] E. W. Michael Lai, David Rubin, *Introduction to Continuum Mechanics*, Fourth Edi, 2009.

[13] T.J. Chung, *Computational Fluid Dynamics*. 2002.

[14] MATLAB, version 7.10.0 (R2017b). Natick, Massachusetts: The MathWorks Inc, 2010.

Appendix

Second order accuracy of finite difference formulations such as central difference, forward, and backward difference for the approximation of **D** and **W** is used. The change of the plane velocity components with respect to both horizontal and vertical direction in the center of the domain is approximated by central difference formulations [5] as

$$\frac{\partial u_{i,j}}{\partial x} = (u_{i\,,\,j+1} - u_{i\,,\,j-1})\ (2\,\Delta x)^{-1}\ ,$$
$$\frac{\partial u_{i,j}}{\partial y} = (u_{i+1\,,\,j} - u_{i-1\,,\,j})\ (2\,\Delta y)^{-1}\ ,$$
$$\frac{\partial v_{i,j}}{\partial x} = (v_{i\,,\,j+1} - v_{i\,,\,j-1})\ (2\,\Delta x)^{-1}\ ,$$
$$\frac{\partial v_{i,j}}{\partial y} = (v_{i+1\,,\,j} - v_{i-1\,,\,j})\ (2\,\Delta y)^{-1}\ .$$

For the domain boundaries, forward and backward difference formulations are used, which forward difference formulations are given by

$$\frac{\partial u_{i,j}}{\partial x} = (-3u_{i\,,\,j} + 4u_{i\,,\,j+1} - u_{i\,,\,j+2})\ (2\,\Delta x)^{-1}\ ,$$
$$\frac{\partial u_{i,j}}{\partial y} = (-3u_{i\,,\,j} + 4u_{i+1\,,\,j} - u_{i+2\,,\,j})\ (2\,\Delta y)^{-1}\ ,$$
$$\frac{\partial v_{i,j}}{\partial x} = (-3v_{i\,,\,j} + 4v_{i\,,\,j+1} - v_{i\,,\,j+2})\ (2\,\Delta x)^{-1}\ ,$$
$$\frac{\partial v_{i,j}}{\partial y} = (-3v_{i\,,\,j} + 4v_{i+1\,,\,j} - v_{i+2\,,\,j})\ (2\,\Delta y)^{-1}\ ,$$

and backward difference formulations are given by

$$\frac{\partial u_{i,j}}{\partial x} = (3u_{i,j} - 4u_{i,j-1} + u_{i,j-2}) (2\,\Delta x)^{-1} ,$$
$$\frac{\partial u_{i,j}}{\partial y} = (3u_{i,j} - 4u_{i-1,j} + u_{i-2,j}) (2\,\Delta y)^{-1} ,$$
$$\frac{\partial v_{i,j}}{\partial x} = (3v_{i,j} - 4v_{i,j-1} + v_{i,j-2}) (2\,\Delta x)^{-1} ,$$
$$\frac{\partial v_{i,j}}{\partial y} = (3v_{i,j} - 4v_{i-1,j} + v_{i-2,j}) (2\,\Delta y)^{-1} .$$

For the approximation of **A** in the horizontal direction, second-order accuracy finite difference formulations are used as

$$\frac{\partial \mathbf{A}_{i,j}}{\partial x} = (\mathbf{A}_{i,j+1} - \mathbf{A}_{i,j-1}) (2\,\Delta x)^{-1} ,$$
$$\frac{\partial \mathbf{A}_{i,j}}{\partial x} = (-3\mathbf{A}_{i,j} + 4\mathbf{A}_{i,j+1} - \mathbf{A}_{i,j+2}) (2\,\Delta x)^{-1} ,$$
$$\frac{\partial \mathbf{A}_{i,j}}{\partial x} = (3\mathbf{A}_{i,j} - 4\mathbf{A}_{i,j-1} + \mathbf{A}_{i,j-2}) (2\,\Delta x)^{-1} .$$